

Silicon Photonic Single-Sideband Generation with Dual-Parallel Mach-Zehnder Modulators for Atom Interferometry Applications

ASHOK KODIGALA, MICHAEL GEHL, GREGORY W. HOTH, JONGMIN LEE, CHRISTOPHER DEROSE, ANDREW POMERENE, CHRISTINA DALLO, DOUGLAS TROTTER, ANDREW L. STARBUCK, GRANT BIEDERMANN, PETER SCHWINDT, AND ANTHONY L. LENTINE

Sandia National Laboratories, 1515 Eubank Blvd SE, Albuquerque, New Mexico 87123 USA
akodiga@sandia.gov

Abstract: We demonstrate a silicon photonic carrier-suppressed single-sideband (CS-SSB) modulator with dual-parallel Mach-Zehnder modulators (DP-MZMs) operating near 1550 nm with a measured carrier suppression of 30 dB and an ultra-high sideband suppression (SSR) of 47.8 dB at 1 GHz with peak conversion efficiency of -6.846 dB (20.7%). We extensively study the effects of imbalances in both the optical and RF phases and amplitudes on the side-band performance. Furthermore, with our silicon photonic modulator, we successfully demonstrate state-selective detection for atoms with time-multiplexed frequency shifting and atom interferometer fringes in a Rubidium (^{87}Rb) atom system to estimate gravitational acceleration. These multidisciplinary efforts demonstrate progress towards an integrated silicon photonic chip-scale laser system for atom interferometry and quantum information science applications.

1. Introduction

In recent years, integrated silicon photonics has matured rapidly to address an increasingly complex and broad application space. The main draw for silicon photonics is its ability to support the integration of complex photonic circuits at the chip-scale by taking advantage of standard complementary metal-oxide-semiconductor (CMOS) fabrication process which can be used for mass production with high yield. With growing demand for silicon photonics, there is a strong need for high performance GHz-scale optical single sideband (SSB) modulators/frequency-shifters on a silicon platform for a variety of applications. These include frequency shifting or conversion for atomic physics research [1-2], radio-over-fiber (RoF) communication systems [3-4], integrated microwave photonics [5-7], light detection and ranging (LIDAR) [8], high-resolution spectroscopy [9-10], and dense wavelength division multiplexed (D-WDM) networks [9]. However, to date, much of SSB work has been concentrated on a lithium niobate (LiNbO_3) platform [11-13]. The few SSB modulators realized on silicon employing resonant ring modulators often lack carrier suppression and are not readily suitable for high-power applications [14-15]. Some realizations on a silicon platform make use of electro-optic polymers which have limited CMOS compatibility and suffer from high optical losses [16]. There are commercially available fiber or free-space acousto-optic modulators (AOMs) which can frequency-shift but are only limited to a few hundred megahertz with gigahertz bandwidths available with significant loss in efficiency [17]. AOMs are also not easily integrated on-chip as they have an angular dependence of the output beam on the modulation frequency which significantly limits bandwidth [18]. Moreover, some of these SSB generation techniques require the filtering of one sideband from a double-sideband (DSB) output via a frequency matched notch or band-reject filter thereby limiting the bandwidth [9]. Another approach is the optical serrodyne modulation of an electro-optic modulator which can in principle achieve wide bandwidths with high efficiencies [19]. However, this is limited by the quality of the sawtooth waveform generated by an expensive arbitrary waveform generator (AWG) and becomes increasingly difficult for high gigahertz bandwidths [20].

In this paper, we design, fabricate, and characterize a silicon photonic CS-SSB modulator using DP-MZM configuration for atom interferometry. For CS-SSB generation, DP-MZMs have also been employed in silicon [21-22]. However, these may not achieve sufficient carrier and sideband suppression needed for atom interferometry [2,23]. In a DP-MZM, the carrier suppression is determined by the careful balancing of the optical amplitudes and phases, whereas sideband suppression is limited by the extinction ratio in each nested-MZM and the RF amplitude/phase balancing. For example, in [21], the RF amplitude imbalance is compensated with an optical power imbalance in each nested-MZM to achieve a high sideband suppression of 39 dB. However, this approach will not achieve peak conversion efficiency as each nested-MZM is asymmetrically driven and also does not compensate for any phase imbalance [24]. Previously, when imbalanced, we achieved a sideband suppression of 12 dB with the use of hybrid RF couplers [25]. In what follows, with careful balancing of the RF amplitude and phase, we show that it's possible to achieve ultra-high sideband suppression of 47.8 dB.

Our multidisciplinary effort, including quantum physics and integrated photonics, reflects the current trend of significant research interest and investment being made in emerging quantum computing and sensing technologies. Of particular interest is a compact laser system composed of integrated photonics for laser cooling and trapping and the atom-light interaction for atom interferometry using state-dependent photon recoils. Deploying atom interferometer inertial sensors requires substantial effort to develop a compact and robust laser system operable at high-dynamic conditions and for the realization of a complete six degree-of-freedom quantum inertial measurement unit (e.g., a 3-axis accelerometer and a 3-axis gyroscope) [26-30]. Current laser systems are mostly based on discrete photonic components that are connected through fiber-to-fiber connections or free-space optical paths with optomechanical alignment mounts, which limit their ability to withstand high dynamics and their ability to be mass-produced. To reduce design complexity and improve reliability, it will be necessary to realize extreme miniaturization of the laser system by integrating nearly all of the many required optical components (*i.e.* modulators, amplifiers, isolators, doublers) onto a single photonic chip [25,31-36]. This chip would use microfabricated optical waveguides spanning material systems and offer robust scalable integrated laser systems that can be mass produced. It is readily envisioned that integrated photonic technology will allow ready scaling from a single axis sensor to a six-degree-of-freedom atom interferometer inertial sensor (three accelerometers and three gyroscope) with a single chip solution. Using integrated silicon photonics, we demonstrate a proof-of-concept atom interferometer where an SC-SSB modulator provides the required light frequencies for state dependent detection and the Raman beams (the beams that form the atom interferometer) in separate experiments. The D2 transition of the Rb atoms (at 780 nm) is particularly amenable to this approach because the optical resonance conveniently matches well with mature silicon photonic technologies for light modulation [25] and optical amplification at 1560 nm before frequency doubling to 780 nm to address the atoms.

2. Design

In what follows, we use a dual-parallel nested MZM configuration to generate a SSB that cancels the unwanted sidebands and simultaneously suppresses the carrier thus alleviating the need for output filters (see Figure 1a) [11]. We have four carrier-depletion phase modulators (in orange) along with multiple TO phase shifters (in blue). The four modulators are split into two pairs of balanced modulators (top and bottom pair). The two balanced modulators are fed optically and electrically in quadrature. Within each arm of a pair, they are π out of phase both optically and electrically. In the un-modulated case, this leads to carrier suppression at the output. In the modulated case, each MZM generates odd harmonics with carrier suppressed at the output. The relative optical phase shift of $\pi/2$ along with the electrical $\pi/2$ phase difference between the top and bottom pairs leads to a relative phase difference in the odd harmonics

generated between the two Mach-Zehnder pairs. When combined, every other odd harmonic interferes constructively ($+1, -3, +5, \dots$). With the suppression of carrier and one of the fundamental sidebands, *i.e.* unwanted sideband, we now have a carrier-suppressed single-sideband optical signal. The complementary harmonics ($-1, +3, -5, \dots$) can either be observed in the adjacent output port or radiated out. With this approach, the conversion efficiency of the carrier into ± 1 sidebands is fundamentally limited to -4.7 dB ($\sim 34\%$) [11]. Additionally, with perfect couplers and phase-shifters, there are no even harmonics. However, in reality, this is not the case and even harmonics are also present.

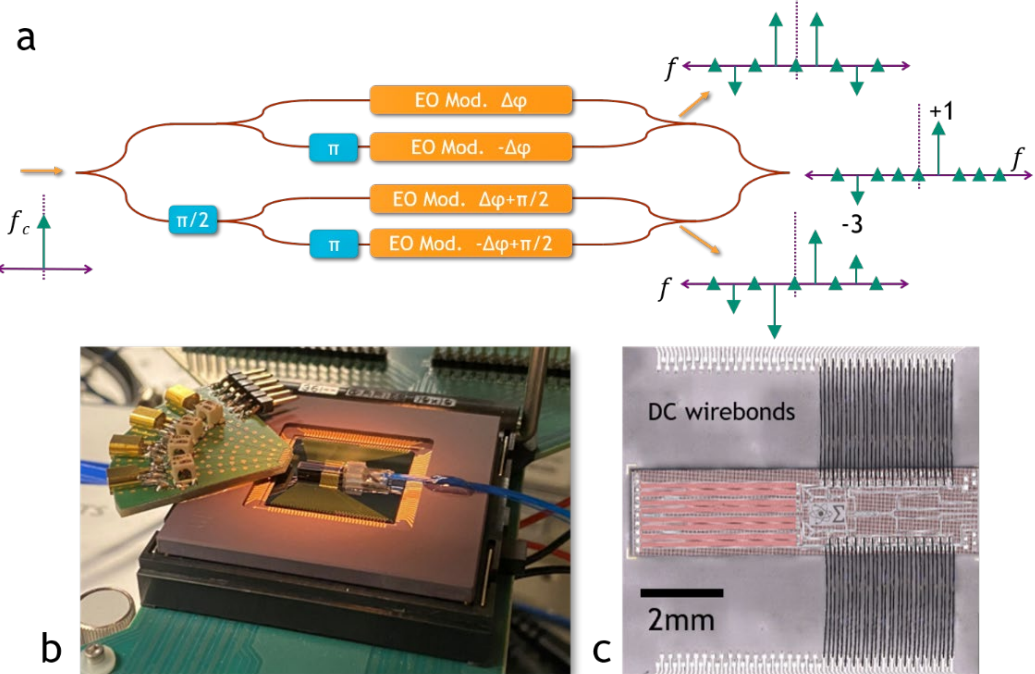


Figure 1: (a) Operational schematic of an optical single-sideband (OSSB) modulator with dual-parallel nested MZMs with required optical phase shifts (in blue) and RF phase offsets (in orange). (b) A packaged, both optically and electrically, one-channel silicon-photonics single-sideband modulator. A v-groove array for optical line and wire bonds for DC and RF to PCB are pictured. (c) Top-view of the fabricated silicon photonic SSB modulator with DC wire bonds to interposer chip with each nested MZM in a push-pull configuration.

Our silicon photonic SSB modulators are fabricated at Sandia's microsystems engineering, science and applications (MESA) complex. Our SSB modulator is packaged both optically and electrically as seen in Figure 1b with a fiber v-groove array, wire bonds to interposer for DC biases, and wire bonds to printed circuit board (PCB) board for RF signal lines. Each nested MZM is configured to be driven in a push-pull configuration with a single RF input thereby needing two RF inputs for the full SSB-modulator. The fabricated chip consists of TO phase shifters to set the optical phases and electro-optic carrier-depletion phase modulators whose active doped modulator region is 1.55 mm in length in each arm (see Figure 1c). The chip has multi-mode interference (MMI) couplers for optical splitters and combiners. The main Mach-Zehnder and the nested MZMs are optically balanced (same path lengths) so there is no wavelength dependence.

3. Experiment results

Figure 2 shows the experimental setup used to test our SSB modulator performance. We test the modulator with a two-channel RF signal source operating at 1 GHz with each channel driving a nested MZM in a push-pull configuration allowing us to independently control the

amplitude and phase of each RF signal. We make use of an RF amplifier for each channel (not pictured). There are three current sources tuning the three TO phase shifters (DC1 to $\pi/2$ and DC2, 3 to π) for optimal optical performance. We make use of a self-heterodyne scheme to characterize our single-sideband modulator, thus we have the needed optical resolution and signal integrity to view all sidebands in the RF domain which is difficult with a scanning Fabry-Perot [25].

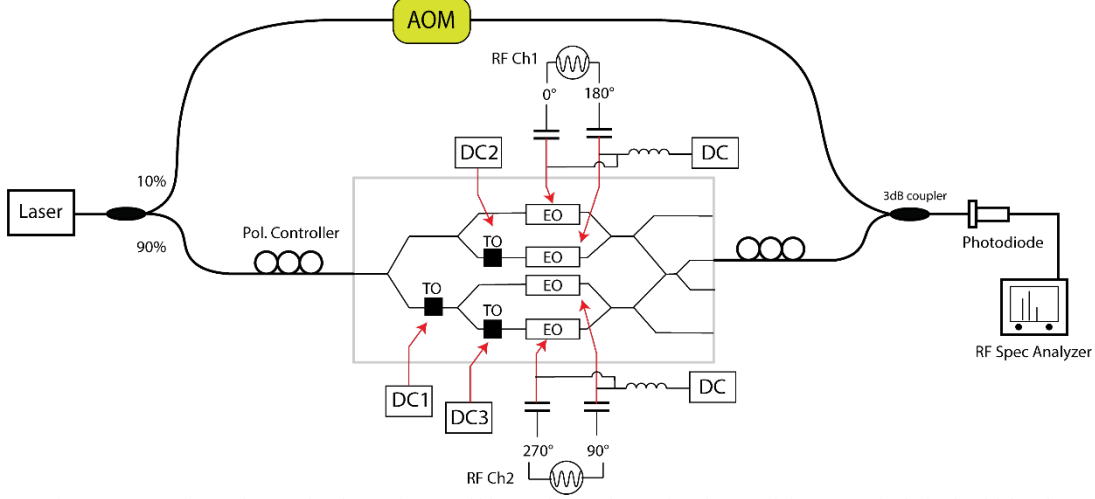


Figure 2: Experimental setup implementing a self-heterodyne scheme for characterizing an optical single-sideband modulator with the input laser at 1550 nm, polarization controllers, acousto-optic modulator (AOM), couplers/splitters, and a photodiode to a RF spectrum analyzer. Modulator is driven by two separate RF channels with each channel driving a nested MZM in push-pull configuration. DC and RF control lines for both TO phase shifters and EO modulators are in red.

We first characterize optical losses in our device. With the RF turned off, we first set our three main DC biases (DC1 to $\pi/2$ and 2, 3 to $-\pi$) to maximize the optical carrier in our side-band port thereby pushing all the carrier through the port of interest. This captures all the optical chip-coupling and propagation losses in our SSB modulator and serves as a normalization for all subsequent sideband measurements. We then proceed to set our biases (DC2, 3 to π) to suppress the carrier in the sideband ports which pushes the carrier to the outer most ports. We suppress the carrier by >40 dB with no RF. This is limited by the extinction of each MZI (~ 30 - 40 dB) and can be further improved to >60 dB each with the use of high-contrast splitters [24, 37-40]. For the remainder of testing, each phase modulator had no reverse-bias.

With the carrier suppressed and RF turned on, we now set both the quadrature phases. We optimize DC1 ($\pi/2$) and the phase of RF-channel 1 relative to 2 ($\pi/2$) with the RF-amplitudes being equal to maximize the extinction between ± 1 sidebands. We then sweep the input RF power in each channel while subtly optimizing DC1 and RF-amplitude of channel 2 together to account for any minor electrical and optical imbalances [21]. The resulting sidebands have Bessel function amplitudes and scale to the order of the sideband with modulation power as seen in Figure 3. Hence, a higher-order sideband has a greater slope. At low RF powers, we observe a remarkable carrier suppression of >40 dB with unwanted sideband suppression exceeding 45dB. The automated optimization briefly fails at high RF powers in this particular sweep and can be improved to maintain unwanted sideband suppression >45 dB. We achieve peak conversion efficiency of -6.846 dB (20.7%) at $+21$ dBm RF-power corresponding to a V_π of ~ 2.5 V in each modulator arm ($V_\pi \cdot L = 0.388$ V·cm). This difference from the efficiency limit of -4.7 dB can be attributed to the lack of reverse-bias in the modulators and inherent non-linearities of the silicon phase modulators [41-42]. The linearity of the modulator can be

improved with reverse-biasing. These non-linearities also contribute to a rise in all other unwanted sidebands irrespective of RF and optical balancing at high RF powers. Moreover, the carrier suppression degrades with increasing RF-power indicating the non-linear nature of the modulators. Ideally, the carrier suppression is independent of RF power or phase and only dependent on the optical amplitude and phases of each MZM. Near peak efficiency at +19 dBm RF-power, we achieve a carrier suppression of 30 dB and extremely high sideband suppression of 47.8 dB. This matches the sideband suppression ratio achieved in a Brillouin laser system of 49 dB [43]. However, the Brillouin approach is limited in tuning bandwidth to a MHz and requires an external pump laser. With reverse-bias and further improvements in RF and optical balancing, we can exceed the carrier and sideband suppression achieved here.

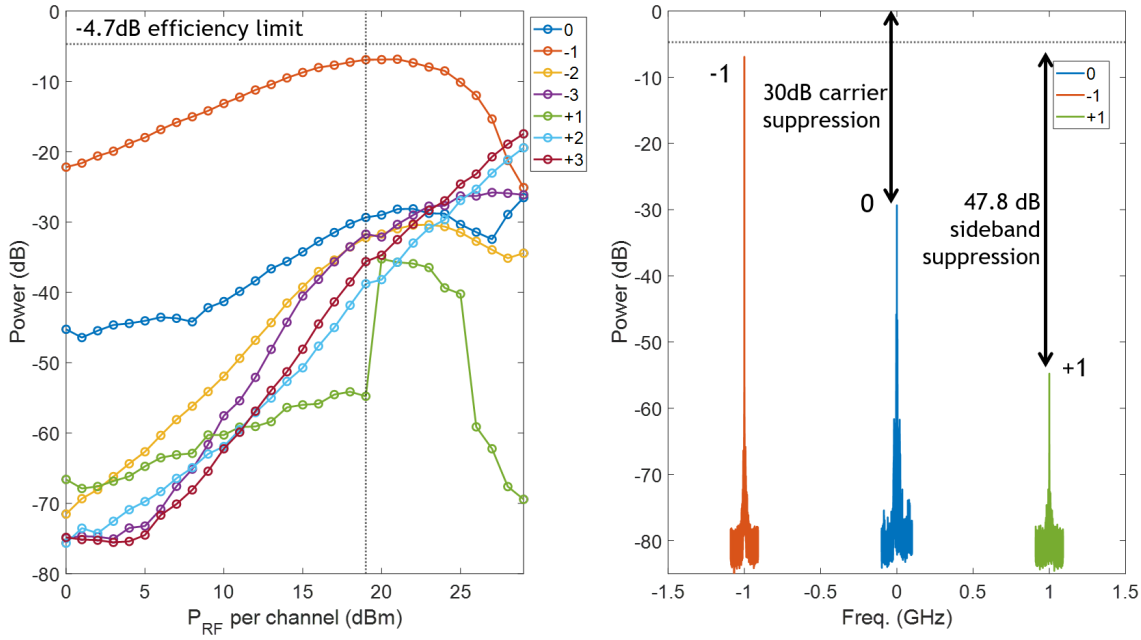


Figure 3: (Left) Measured optical powers of suppressed-carrier (0) and sidebands ($\pm 1, \pm 2, \pm 3$) as a function of RF drive power in each channel. All powers normalized to the total on-chip carrier accounting for optical coupling losses. Peak conversion efficiency of -6.84 6dB (20.7%) is achieved at +21 dBm RF-power corresponding to a V_π of ~ 2.5 V in each modulator arm ($V_\pi L = 0.388$ V·cm). At higher RF powers, non-linearities in the silicon modulators contribute to a rise in all other unwanted sidebands irrespective of RF balancing. (Right) Spectra of carrier and ± 1 sidebands with carrier suppression of 30 dB and sideband suppression of 47.8 dB at +19 dBm RF-power (vertical dotted line in left).

We further explore the effects of both RF amplitude and RF phase imbalances on modulator performance. These RF imbalances are very typical of commercial hybrid couplers (both 90° and 180°) and often limit performance. We once again optimize the modulator for sideband extinction at a RF power of +10 dBm in each channel with RF phase at quadrature and introduce an amplitude imbalance in one channel (see Figure 4). We model an ideal SSB modulator with an amplitude (power) imbalance between RF channels. As expected, only the ± 1 and ± 3 sidebands are present with the carrier fully suppressed. We observe a severe degradation in sideband extinction as RF amplitudes are un-equal. For a sideband suppression < 40 dB, the imbalance needs to be within ± 0.2 dB according to the model. We also experimentally observe this degradation in sideband extinction with amplitude imbalance while achieving > 45 dB sideband suppression.

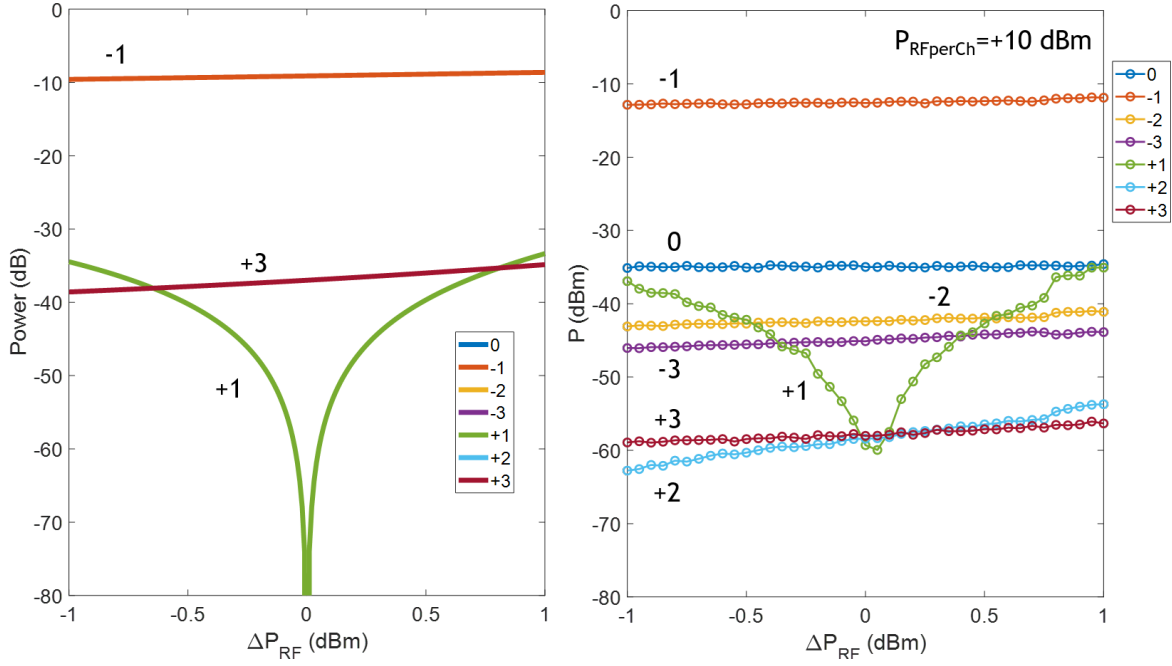


Figure 4: (Left) Model of an ideal SSB modulator operation with an amplitude (power) imbalance between RF channels at a starting RF power in each channel of +10 dBm with RF phase at quadrature. Only the ± 1 and $+3$ sidebands are present in the ideal model as the carrier and other sidebands are completely suppressed. For a sideband suppression < 40 dB, the imbalance needs to be within ± 0.2 dB. (Right) Measured optical powers of suppressed-carrier (0) and all sidebands ($\pm 1, \pm 2, \pm 3$) as a function of RF amplitude imbalance. For both model and measurement, we observe a severe sensitivity to amplitude imbalance on sideband suppression. We achieve a sideband suppression of > 45 dB when perfectly balanced.

Next, we introduce a phase imbalance from quadrature with balanced RF amplitudes. Note that all the optical phases are still optimized for carrier suppression and maximum sideband. We observe both in model and experimentally the tight tolerance of $\pm 5^\circ$ in phase for sideband suppression > 30 dB (see Figure 5). We also note that the ± 1 sidebands switch at 180° as expected in the model, however experimentally this happens at $\sim 230^\circ$ instead. The $+1$ -sideband curve is shifted from its expected and needs further investigation.

Overall, there is excellent agreement between the model and experiments for RF balancing. We hope to improve the peak efficiency of the SSB modulator by reverse-biasing the modulators. In terms of optical balancing, the use of high-contrast splitters or cascaded MZMs will drastically improve the present carrier-suppression by increasing the extinction of each MZM. Along with the carrier, this also improves suppression of all even-harmonics (± 2 sidebands). Moreover, the optical phases can be self-biasing with the implantation of an active feedback scheme operating in conjunction with integrated germanium (Ge) detectors as power monitors [44]. As for RF balancing, we have assumed here that a pair of phase-modulators in each MZM are driven perfectly out-of-phase (π) in a push-pull configuration. In reality, this is not the case due to the inherent non-linearity of these carrier-depletion phase modulators with bias. Our modelling indicates that a deviation from π will adversely affect even-harmonics (± 2 sidebands suppression) including the carrier-suppression. This could be overcome with the use of a single-drive configuration where each modulator is independently driven but this comes at the cost of added complexity of having four RF channels to balance instead of two.

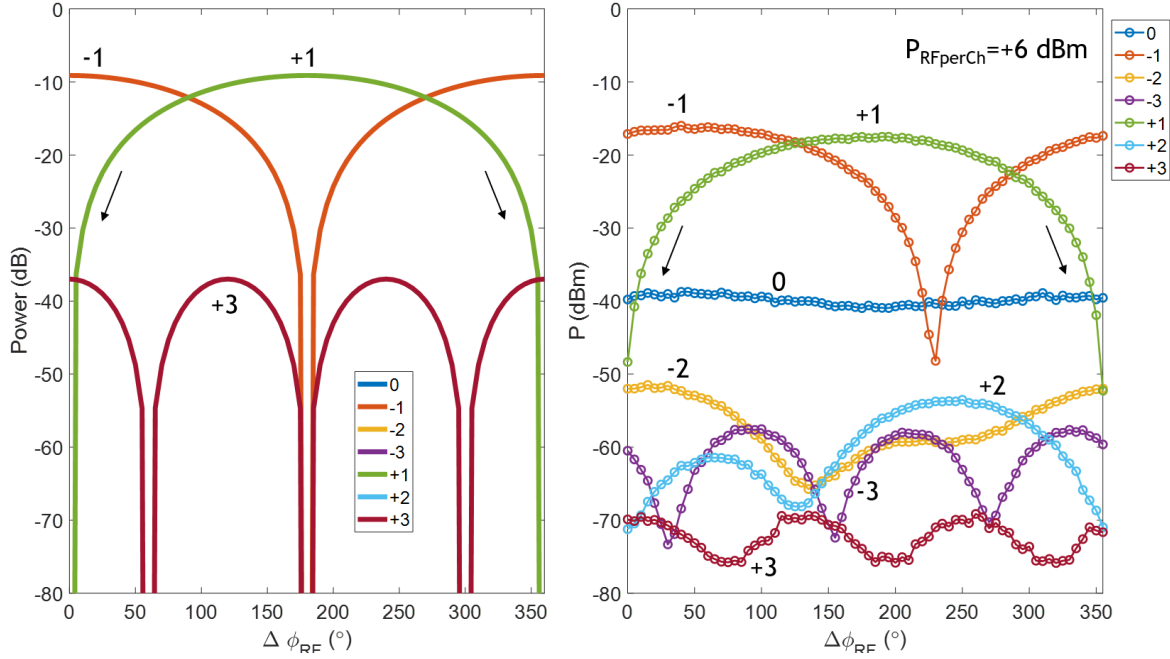


Figure 5: (Left) Model of an ideal SSB modulator operation with a phase imbalance between RF channels from quadrature with a RF power in each channel of +6 dBm. As expected, the ± 1 sidebands switch at 180° with only $\pm 5^\circ$ tolerance for sideband suppression > 30 dB. (Right) Measured optical powers of suppressed-carrier (0) and all sidebands ($\pm 1, \pm 2, \pm 3$) as a function of RF phase imbalance. There is overall very good agreement with the model, however the phase at which the sidebands switch is at $\sim 230^\circ$ instead of 180° which needs further exploration.

4. State-selective detection and atom interferometry demonstration

In what follows, we make use of our silicon photonic CS-SSB modulator to validate functionality towards quantum inertial sensing by demonstrating state-selective detection and atom interferometry. In contrast, a typical electro-optic phase modulator produces a double-sideband spectrum and does not suppress the carrier. The presence of any unwanted sideband will introduce parasitic transitions and unwanted light shifts, which impair the performance of an atom interferometer [1, 45].

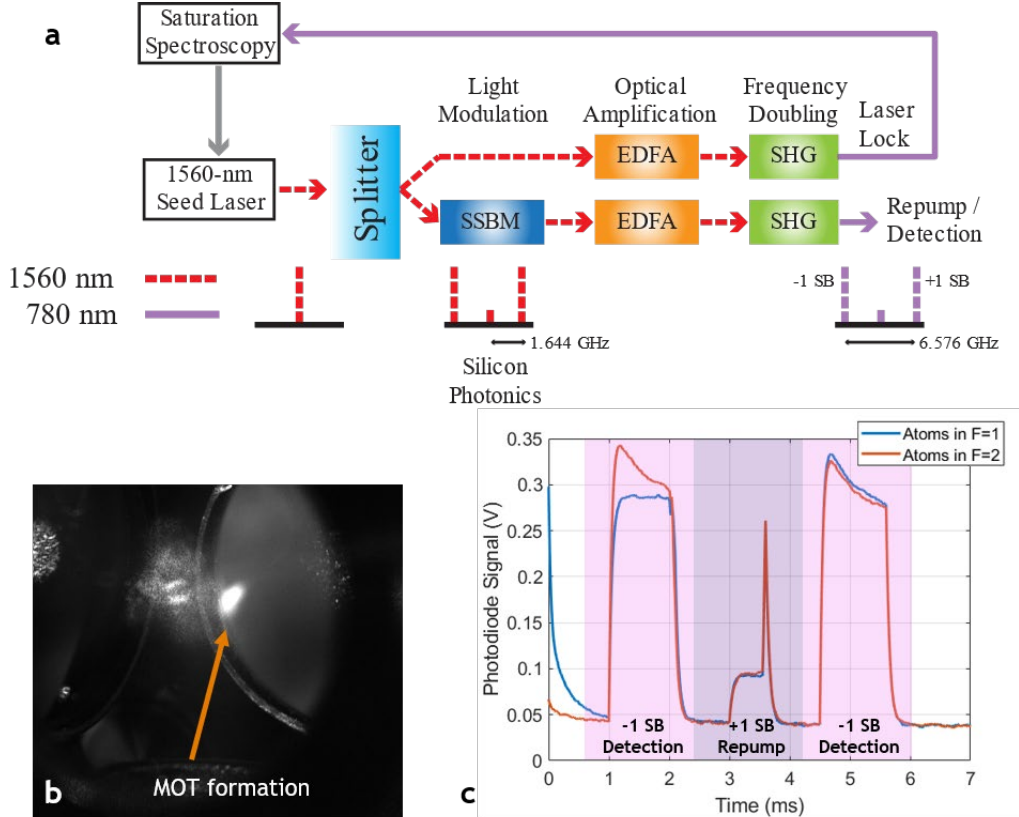


Figure 6: (a) Experimental setup of state-selective detection for atoms using the silicon photonic SSB modulator (SSBM) chip which can switch the modulation frequency between ± 1.644 GHz sidebands at 1560 nm to generate repump and detection (or cooling) beams at 780 nm for Rb atoms, where EDFA is an erbium-doped fiber amplifier and SHG is a second harmonic generator. (b) A picture of a Rb magneto-optic trap (MOT) through simultaneous generation of repump and cooling beams at 780 nm. (c) Demonstration of state-selective detection for atoms in the initial state of $F=1$ (blue) or $F=2$ (red). On-chip TO phase shifter (response time = ~ 20 μ s) is used to switch between $+1$ and -1 sidebands. The master laser is locked at the midpoint of detection and repump frequencies. Hence, the total frequency jump at 780 nm is 6.576 GHz.

As shown in Figure 6a, the laser system uses a single master/seed laser at 1560 nm. The 1560 nm laser is frequency-doubled and locked to an atomic transition using saturation spectroscopy. The silicon photonic SSB modulator produces repump and detection (or cooling) beams in a simultaneous or time-multiplexed manner at 780 nm for the cold-atom system in conjunction with an erbium-doped fiber amplifier (EDFA) and a second harmonic generator (SHG) or doubler, where the SSB modulator is driven at 1.644 GHz at 1560 nm. Simultaneous generation of repump and cooling beams at doubled 780 nm signal can generate a Rb magneto-optic trap (MOT) (see Figure 6b).

With the MOT, we demonstrate state-selective detection for atoms in the initial state of $F=1$ or $F=2$ by sequentially generating detection, repump, and detection beams as shown in Figure 6c. For this experiment (and the MOT demonstration), the 1560-nm laser is locked between the two ^{87}Rb transitions. An on-chip TO phase shifter is used to switch the output optical frequency between the $+1$ sideband (repump) and the -1 sideband (detection) with the total frequency jump at 780 nm being 6.576 GHz. In the first pulse of detection beam (-1 sideband), the atoms are illuminated with light resonant with the $F=2$ to $F'=3$ transition in ^{87}Rb , which causes atomic fluorescence with the $F=2$ hyperfine-ground-state atoms. The SSB modulator chip is DC-biased through TO phase shifters to output the sideband shifted down in frequency (-1 sideband).

Depending on the initial state of the atoms, we can see a clear difference in the number of photons scattered. In the second pulse, the light is resonant with the $F=1$ to $F'=2$ repump transition, which rapidly pumps atoms from the $F=1$ hyperfine state up to the $F=2$ level. Between the first and second pulses, the DC bias of the SSB modulator chip is changed dynamically with a single TO phase shifter so that the chip outputs the sideband shifted up in frequency (+1 sideband). For the third pulse, the TO phase shifters are switched back such that the -1 sideband is output, and the detection beam is again resonant with the $F=2$ to $F'=3$ transition. In the third pulse, essentially all the atoms are in the $F=2$ state and thus can be used as a normalization signal for the first pulse. In the pulse sequence of state-selective detection, the bias or sideband switching corresponds to switching the quadrature optical phase between $\pi/2$ and $3\pi/2$, and the intensity spike at the end of the second pulse is caused by the sudden change in the bias current. In atom interferometry, state-selective detection is needed to observe the atom interferometer fringes based on atomic population and measure the phase shifts of interest for acceleration and angular rate sensing [46]. This demonstration validates the function of the silicon photonic SSB modulator capable of dynamically modulating the light frequency during a single cycle of a cold-atom system, such as in an atom interferometer.

As a second demonstration of the capabilities of the silicon photonic SSB modulator, we use our SSB modulator to produce Doppler-sensitive Raman beams through stimulated Raman transitions that coherently address atomic states and deliver state-dependent photon recoils for matter-wave interference [46]. The stimulated Raman transitions require two phase-coherent frequency components, separated by the atomic hyperfine splitting, which is $f_{\text{hfs}} \approx 6.834$ GHz for ^{87}Rb (see Figure 7). The modulator chip is modulated at $f_{\text{hfs}}/2$ to produce a single-sideband light at 780 nm shifted by f_{hfs} after optical amplification (1560 nm) and frequency doubling (1560 to 780 nm). We simply combined this sideband with an amplified and frequency-doubled carrier frequency (offset-locked to a repump transition with -1 GHz detuning) which is obtained from another channel of the SSB modulator chip without modulation. Two Raman beams combined in a Lin-perp-Lin polarization configuration, which are simultaneously switched using an AOM, are sent to a sample of cold atoms prepared in our vacuum chamber. In order to control phase shifts due to changes in the independent paths of the two frequency components, we stabilized the relative phase of the Raman tones by detecting a beat note between the tones and implementing a phase-locked loop that feeds back to the RF source driving the SSB modulator.

An atom interferometer can be realized with a sequence of three Raman pulses that drive stimulated Raman transitions [46]. The light-pulse sequence $(\pi/2 \rightarrow T \rightarrow \pi \rightarrow T \rightarrow \pi/2)$ splits, redirects, and recombines atomic wave-packets for matter-wave interference analogous to an optical Mach Zehnder interferometer (50/50 beam splitter \rightarrow mirror \rightarrow 50/50 beam splitter), where a $\pi/2$ Raman pulse coherently splits/recombines atomic wave-packets with state-dependent photon recoils, a π Raman pulse redirect atomic wave-packets by reversing both the atomic states and the atomic momentum where T is the interrogation time. At the end of atom interferometer operation, the atom interferometer fringe corresponds to the atomic population of two hyperfine-ground-states of the atoms. As the relative phase between the two interferometric branches is varied, the atom interferometer fringe oscillates. In our experiments, we varied the atom interferometer phase by scanning the time, T , between the Raman pulses ($T = 0$ to T'). Under acceleration due to gravity, a sinusoidal atom interferometer fringe becomes chirped due to Doppler-shifted atomic resonance with respect to Doppler-sensitive Raman beams. With this approach, the fraction of the atoms in the upper hyperfine state is described by $P \approx P_0 + \frac{c}{2} \cos \left(k g \tau_\pi \left(1 + \frac{2}{\pi} \right) T + k g T^2 \right)$ where P_0 is an offset, c is the interferometer contrast, τ_π is the duration of the mirror pulse, k is the effective wave number for the Raman transitions, and g is the local acceleration due to gravity [47]. The chirped atom interferometer fringes are obtained using a laser system that includes the silicon photonic SSB modulator (see

Figure 7, Bottom). Neither demo was performed at the best SSB modulator performance achieved in the previous section and is an active topic of future study.

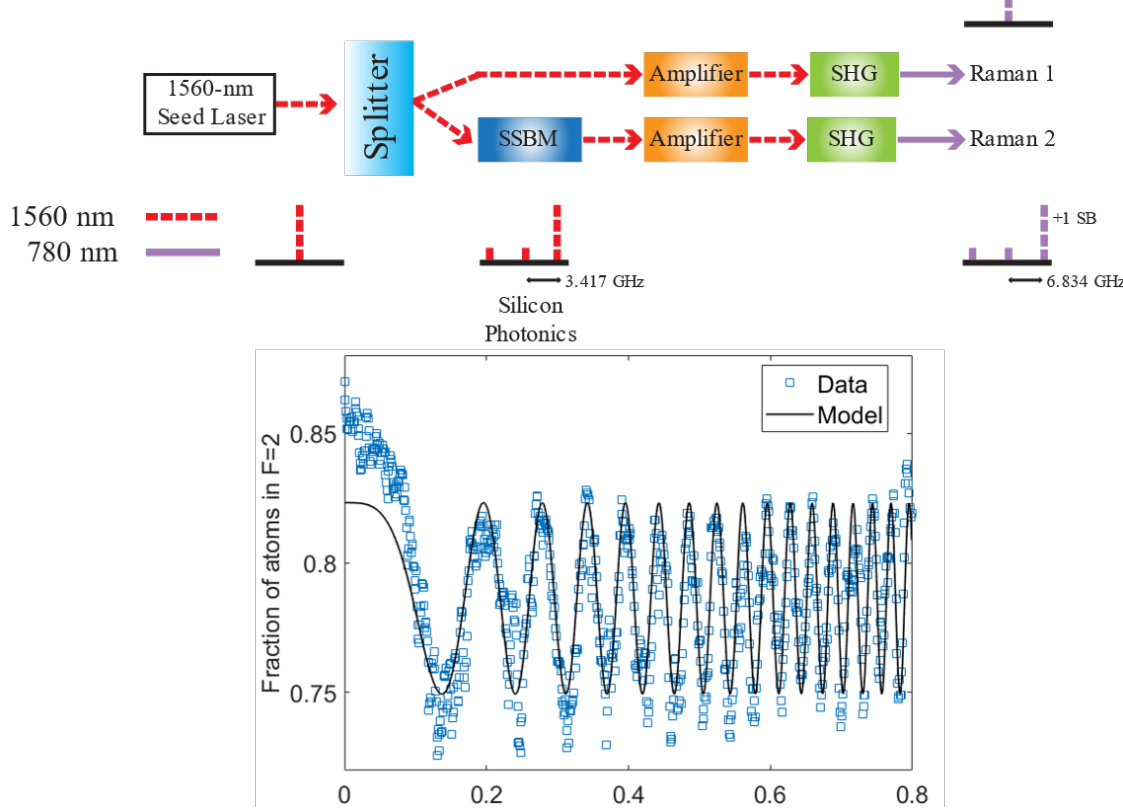


Figure 7: (Top) Experimental setup of Doppler-sensitive Raman beams for atom interferometry using the silicon photonic SSB modulator chip which operates at +3.417 GHz at 1560 nm (+6.834 GHz at 780 nm once doubled). (Bottom) Atom interferometer fringes produced with the silicon photonic SSB modulator chip. The data has been smoothed with a four-point running average. The Raman pulse duration was $\tau_\pi = 5 \mu\text{s}$. The estimated local gravitational acceleration is $g \approx 9.77 \pm 0.01 \text{ m/s}^2$, where the error is one standard deviation, as estimated by the nonlinear least-squares fitting routine.

Although much work remains to be done to obtain atom interferometer fringes with high signal-to-noise ratio and stable fringe amplitude, this initial demonstration of coherent atomic interference fringes indicates the silicon photonic SSB modulator is a promising tool for compact atom-interferometer systems. Furthermore, by integrating multiple SSB modulators onto a single chip with suppressed carrier and unwanted sidebands, our silicon photonic SSB modulator chip has the potential to simplify laser systems for atom interferometry and eliminate unwanted systematics. Moreover, with further improvements in optical losses and additional on-chip integration of optical amplifiers, isolators, and doublers, the above atom interferometry laser setup can be fully miniaturized onto a single chip enabling compact quantum inertial sensors.

5. Conclusion

We have demonstrated an optical SSB modulator based on dual-parallel MZMs on a silicon platform with high carrier (30 dB) and ultra-high sideband (47.8 dB) suppression near the peak efficiency point of -6.846 dB (20.7%). We achieved such high suppression with careful balancing of optical and RF phases and amplitudes. We note that even higher carrier suppression can be achieved with the use of high-contrast optical splitters. Moreover, we show

that the sideband suppression is highly sensitive to the RF amplitude and phase balance between channels in a push-pull or dual-drive configured SSB modulator. The frequency shift of the SSB modulator is in principal variable and limited to the frequency response of the modulator. With further refinement using travelling wave electrodes, our SSB modulator should be operational beyond 20 GHz [48-49]. We also note that the principles of SSB operation outlined here apply to a different material system such as thin-film lithium-niobate which allows for even larger bandwidths and is more linear than silicon [31,50]. Furthermore, we have demonstrated state-selective detection and a Rb MOT using our silicon photonic SSB modulator chip showing the capability of dynamically shifting between the ± 1 sidebands or simultaneously driving both sidebands during a single cycle of a cold-atom system. Lastly, our SSB modulator chip was successfully used in an atom interferometer system to measure gravitational acceleration. This enables the miniaturization of many complicated atomic or photonic systems into a chip-scale integrated solution.

Funding/Acknowledgments/Disclosure

This work is supported by the Laboratory Directed Research and Development program at Sandia National Laboratories, a multi-mission laboratory managed and operated by National Technology & Engineering Solutions of Sandia, LLC, a wholly owned subsidiary of Honeywell International Inc., for the U.S. Department of Energy's National Nuclear Security Administration under contract DE-NA0003525. This paper describes technical results and analysis. Any subjective views or opinions that might be expressed in the paper do not necessarily represent the view of the U.S. Department of Energy or the United States Government. We wish to thank Nicholas Boynton for help with packaging and Nils Otterstrom for fruitful discussions. SAND2022-5279 O

References

1. L. Zhu, Y-H. Lien, A. Hinton, A. Niggebaum, C. Rammeloo, K. Bongs, and M. Holynski, "Application of optical single-sideband laser in Raman atom interferometry," *Optics Express* **26**, 6542 (2018).
2. C. Rammeloo et al., "Performance of an optical single-sideband laser system for atom interferometry," *JOSAB* **37**, 5 (2020).
3. Y. Tong et al., "Integrated silicon photonics remote radio frontend (RRF) for single-sideband (SSB) millimeter-wave radio-over-fiber (ROF) systems," *J. IEEE Photon* **11**, 2 (2019).
4. C. W. Chow et al., "Long-reach radio-over-fiber signal distribution using single-sideband signal generated by a silicon-modulator," *Opt. Express* **19**, (2011).
5. D. Marpaung, C. Roeloffzen, R. Heideman, A. Leinse, S. Sales, and J. Capmany, "Integrated microwave photonics," *Laser Photonics Rev* **7** (4), 506-538 (2013).
6. D. Marpaung, J. Yao, and J. Capmany, "Integrated microwave photonics," *Nature Photonics* **13**, 80-90 (2019).
7. R. Maram, S. Kaushal, J. Azaña, L.R. Chen, "Recent Trends and Advances of Silicon-Based Integrated Microwave Photonics," *Photonics* **6**, 13 (2019).
8. M. Kamata, Y. Hinakura, and T. Baba, "Carrier-suppressed single sideband signal for FMCW LiDAR using a Si photonic-crystal optical modulators," *J. Lightwave. Technol.* **38**, 8 (2020).
9. L. T. Nichols and R. D. Esman, "Single sideband modulation techniques and applications," *OFC/IOOC* **3**, 332 (1999).
10. T. Shioda, K. Fujii, K. Kashiwagi, and T. Kurokawa, "High-resolution spectroscopy combined with the use of optical frequency comb and heterodyne detection," *J. Opt. Soc. Am. B* **27**, 1487-1491 (2010).
11. M. Izutsu, S. Shikama, and T. Sueta, "Integrated Optical SSB Modulator/Frequency Shifter," *IEEE J. Quantum Electron.* **17**, 11 (1981).
12. S. Shimotsu, S. Oikawa, T. Saitou, N. Mitsugi, K. Kubodera, T. Kawanishi, and M. Izutsu, "Single Side-Band Modulation Performance of a LiNbO₃ Integrated Modulator Consisting of Four-Phase Modulator Waveguides," *IEEE Photon. Technol. Lett.* **13**, 4 (2001).
13. Y. Hu et al, "On-chip electro-optic frequency shifters and beam splitters," *Nature* **599**, 587-593 (2021).
14. S. Song, X. Yi, S. X. Chew, L. Li, L. Nguyen, and R. Zheng, "Optical single-sideband modulation based on silicon-on-insulator coupled-resonator optical waveguides," *Optical Engineering* **55** (3), 031114 (2015).
15. B-M. Yu, J-M. Lee, C. Mai, S. Lischke, L. Zimmermann, and W-Y. Choi, "Single-chip Si Optical single-sideband modulator," *Photon. Res.* **6**, 1 (2018).
16. M. Lauermann, C. Weimann, A. Knopf, W. Heni, R. Palmer, S. Koeber, D. L. Elder, W. Bogaerts, J. Leuthold, L. R. Dalton, C. Rembe, W. Freude, and C. Koos, "Integrated optical frequency shifter in silicon-organic hybrid (SOH) technology," *Optics Express* **24**, 11694-11707 (2016).
17. N. Savage, "Acousto-optic devices," *Nature Photonics* **4**, 728 (2010).
18. C. S. Tsai, "Integrated acousto-optic and magneto-optic Bragg cell modulators and their applications," *Opt. Eng.* **38**, 7 (1999).

19. L. M. Johnson and C. H. Cox, "Serrodyne optical frequency translation with high sideband suppression," *J. Lightwave Technol.* **6**(1), 109–112 (1988).
20. D. M. S. Johnson, J. M. Hogan, S.-w. Chiow, and M. A. Kasevich, "Broadband optical serrodyne frequency shifting," *Optics Letters* **35**, 745 (2010).
21. P. Xia et al., "A silicon optical single sideband modulator with ultra-high sideband suppression ratio," *IEEE Photonics Technology Letters* **32**, 963-966 (2020).
22. P. Shi et al., "Optical single-sideband modulation based on a silicon dual-parallel Mach-Zehnder modulator," *Asia Comm and Photonics Conf.* (2020).
23. J. Lee et al, "A compact cold-atom interferometer with a high data-rate grating magneto-optical trap and a photonic-integrated-circuit-compatible laser system," *arxiv* 2107.04792v2 (2021).
24. Y. Ogiso, Y. Tsuchiya, S. Shinada, S. Nakajima, T. Kawanishi, H. Nakajima, "High Extinction-Ratio Integrated Mach-Zehnder Modulator with Active Y-Branch for Optical SSB Signal Generation," *IEEE Photon. Technol. Lett.* **22**, 12 (2010).
25. A. Kodigala, M. Gehl, C. T. DeRose, D. Hood, A. T. Pomerene, C. Dallo, D. Trotter, P. Moore, A. L. Starbuck, J. Lee, G. Biedermann, and A. L. Lentine, "Silicon Photonic Single-Sideband Generation with Dual-Parallel Mach-Zehnder Modulators," In *Conference on Lasers and Electro-Optics*, STh4N.6, DOI: 10.1364/CLEO_SI.2019.STh4N.6 (Optical Society of America, 2019).
26. Lévéque, T., Antoni-Micollier, L., Faure, B. et al. A laser setup for rubidium cooling dedicated to space applications. *Appl. Phys. B* **116**, 997–1004 (2014).
27. Schkolnik, V., Hellmig, O., Wenzlawski, A. et al. A compact and robust diode laser system for atom interferometry on a sounding rocket. *Appl. Phys. B* **122**, 217 (2016).
28. Caldani, R., Merlet, S., Pereira Dos Santos, F. et al. A prototype industrial laser system for cold atom inertial sensing in space. *Eur. Phys. J. D* **73**, 248 (2019).
29. Sabulsky, D.O., Junca, J., Lefèvre, G. et al. A fibered laser system for the MIGA large scale atom interferometer. *Sci Rep* **10**, 3268 (2020).
30. Frye, K., Abend, S., Bartosch, W. et al. The Bose-Einstein Condensate and Cold Atom Laboratory. *EPJ Quantum Technol.* **8**, 1 (2021).
31. N. Boynton et al., "A heterogeneously integrated silicon photonic/lithium niobate travelling wave electro-optic modulator," *Opt. Express* **28**, 1868-1884 (2020).
32. Kittlaus, E. A., Shin, H., & Rakich, P. T. (2016). Large Brillouin amplification in silicon. *Nature Photonics*, **10**(7), 463–467.
33. Otterstrom, N. T. et al. Resonantly enhanced nonreciprocal silicon Brillouin amplifier. *Optica* **6**, 1117–1123 (2019).
34. Weigel, P. O. et al. Bonded thin film lithium niobate modulator on a silicon photonics platform exceeding 100-GHz 3-dB electrical modulation bandwidth. *Opt. Express* **26**, 23728–23739 (2018).
35. J. Zhao, et al., "Shallow-etched thin-film lithium niobate waveguides for highly-efficient second-harmonic generation," *Opt. Express* **28**, 19669-19682 (2020).
36. K. Van Gasse, Ruijun Wang, and Gunther Roelkens, "27 dB gain III-V-on-silicon semiconductor optical amplifier with > 17 dBm output power," *Opt. Express* **27**, 293-302 (2019).
37. K. Suzuki, G. Cong, K. Tanizawa, S.-H. Kim, K. Ikeda, S. Namiki, and H. Kawashima, "Ultra-high-extinction ratio 2×2 silicon optical switch with variable splitter," *Opt. Express* **23**(7), 9086–9092 (2015).
38. C. M. Wilkes, X. Qiang, J. Wang, R. Santagati, S. Paesani, X. Zhou, D. A. B. Miller, G. D. Marshall, M. G. Thompson, and J. L. O'Brien, "60 dB high-extinction auto-configured Mach-Zehnder interferometer," *Opt. Lett.* **41**(22), 5318–5321 (2016).
39. S. Liu, H. Cai, C. T. DeRose, P. Davids, A. Pomerene, A. L. Starbuck, D. C. Trotter, R. Camacho, J. Urayama, and A. Lentine, "High speed ultra-broadband amplitude modulators with ultrahigh extinction >65dB," *Opt. Express* **25**, 10 (2017).
40. H. Cai, S. Liu, A. Pomerene, D. C. Trotter, A. L. Starbuck, C. Dallo, D. Hood, C. T. DeRose, and A. L. Lentine, "A stable ultrahigh extinction silicon photonic amplitude modulator," *Optical Interconnects Conference* (2018).
41. C. G. Bottemfield, V. A. Thomas, and S. E. Ralph, "Silicon photonic modulator linearity and optimization for microwave photonic links," *IEEE J. Sel. Top. Quantum Electron.* **25**, 3400110 (2019).
42. Q. Zhang, H. Yu, H. Jin, T. Qi, Y. Li, J. Yang, and X. Jiang, "Linearity comparison of silicon carrier-depletion-based single, dual-parallel, and dual-series Mach-Zehnder modulators," *J. Light. Technol.* **36**, 3318 (2018).
43. N. T. Otterstrom et al, "Backscatter-Immune Injection-Locked Brillouin Laser in Silicon," *Phys. Rev. Applied* **14**, 044042 (2020).
44. C. T. DeRose, D. C. Trotter, W. A. Zortman, A. L. Starbuck, M. Fisher, M. R. Watts, and P. S. Davids, "Ultra compact 45 GHz CMOS compatible Germanium waveguide photodiode with low dark current," *Optics Express* **19**, 24898 (2011).
45. G. W. Biedermann, H. J. McGuinness, A. V. Rakholia, Y.-Y. Jau, D. R. Wheeler, J. D. Sterk, and G. R. Burns, "Atom interferometry in warm vapor," *Phys. Rev. Lett.* **118**, 163601 (2017).
46. M. Kasevich and S. Chu, "Atomic Interferometry Using Stimulated Raman Transitions," *Phys. Rev. Lett.* **67** 181 (1991).
47. H. J. McGuinness, A. V. Rakholia, and G. W. Biedermann, "High data-rate atom interferometer for measuring acceleration," *Appl. Phys. Lett.*, **100** 011106 (2012).
48. J. Witzens, "High-Speed Silicon Photonics Modulators," in *Proceedings of the IEEE* **106**, 2158-2182 (2018).

49. C. T. DeRose *et al.*, “High speed travelling wave carrier depletion silicon Mach Zehnder modulator,” Opt. Interconnects Conf. 135-36 (2012).
50. X. Huang X *et al.*, “Linearity-Enhanced Dual-Parallel Mach-Zehnder Modulators Based on a Thin-Film Lithium Niobate Platform,” Photonics 9(3)197 (2022).